This article has been accepted for publication in a future issue of this journal, but has not been fully edited. Content may change prior to final publication. Citation information: DOI 10.1109/TEC.2018.2812181, IEEE Transactions on Energy Conversion

Control of a Three-Phase Hybrid Converter for a PV Charging Station

Ahmad Tazay, *Student Member, IEEE,* Zhixin Miao, *Senior Member, IEEE*

***Abstract*—Hybrid boost converter (HBC) has been proposed to replace a dc/dc boost converter and a dc/ac converter to reduce conversion stages and switching loss. In this paper, control of a three-phase HBC in a PV charging station is designed and tested. This HBC interfaces a PV system, a dc system with a hybrid plug-in electrical vehicles (HPEVs) and a three-phase ac grid. The control of the HBC is designed to realize maximum power point tracking (MPPT) for PV, dc bus voltage regulation, and ac voltage or reactive power regulation. A testbed with power electronics switching details is built in MATLAB/SimPowersystems for validation. Simulation results demonstrate the feasibility of the designed control architecture. Finally, lab experimental testing is conducted to demonstrate HBC's control performance.**

***Index Terms*—Plug-in hybrid vehicle (PHEV), Vector Control, Grid-connected Photovoltaic (PV), Three-phase Hybrid Boost Converter, Maximum Power Point Tracking (MPPT), Charging Station.**

I. INTRODUCTION

THE environmental and economic advantages of PHEV lead to the increase in number of production and consumption [1]. The U.S. Department of Energy forecasts that over one million PHEVs will be sold in the U.S. during the next decade [2]. Research has been conducted on developing a charging station by integrating a three-phase ac grid with PHEVs [3]–[5]. The comparison of different PHEV chargers' topologies and techniques are reviewed in [1], [6]. However, a large-scale penetration of PHEVs may add more pressure on the grid during charging periods. Therefore, charging stations with PV as an additional power source become a feasible solution.

For PV charging stations, [7] proposed an architecture and controllers. The charging management is developed in [8] by considering the grid's loading limit. For this type of systems, it requires controlling at least three different power electronic converters to charge PHEVs. Each converter needs an individual controller, which increases complexity and power losses of the system. Consequently, it is urgent to investigate multi-port converters to reduce the number of converting stages.

The objective of the paper is to implement such a multi-port converter in a PV charging station for PHEVs and design the controller.

A. Related Works

In order to decrease the number of switching stages, the inverse Watkins-Johnson technique is proposed in [9] by supplying power simultaneously to dc and ac loads. Single-phase and three-phase of hybrid boost converters (HBC) that can integrate a dc power source, dc loads and ac loads for a microgrid are proposed in [10] and [11], respectively. Recent research in [12] also suggests that a hybrid single-phase converter can be applied in grid-connected applications.

All previous research on HBC controller design [10]–[12] assumes that the hybrid converter is connected to a stiff dc voltage source. Hence, the function of maximum power point tracking (MPPT) for PV systems is not yet developed for HBC. Although MPPT algorithm exists in the literature, the application is mainly for a dc/dc converter (e.g., [13]) or a dc/ac converter (e.g., [14]). Implementation of MPPT in HBC has not been investigated. This implementation is not a trivial problem since it requires a thorough understanding on HBC switching mechanism and the coordination of MPPT function and the vector control function.

B. Our Contributions

This paper proposes control design and power management for a PV charging station for PHEV by use of a three-phase HBC. The PV charging station charges PHEVs using power from PV and/or the ac grid. The three-phase HBC integrates three main elements of the system: PV, PHEV and the grid. Control design will be presented in detail. The control will enable PV maximum power point tracking (MPPT) and dc voltage control regulation for PHEVs.

Our contributions lie in two aspects. The *first* contribution is modeling of a PV charging station based on a three-phase HBC that integrates PV arrays, PHEVs, and a utility grid. This novel topology of PV charging station, to the best of authors' knowledge, has not yet been seen in the literature. The advantage of the HBC based PV charging station is the reduction of the number of power conversion stages and losses. The existing PV charging station requires controlling at least three converters including a dc boost converter for MPPT algorithm, a three-phase dc/ac inverter, and a dc converter for battery's charging [15]. Instead, the HBC integrates the first dc boost converter and the dc/ac three-phase inverter into a single structure.

The *second* contribution is the design of the HBC controller. Existing controllers for HBC [10]–[12] have not included MPPT function since the dc input side is assumed as a stiff dc voltage in the aforementioned research. In our research, we consider the details related to the PV and further implemented MPPT algorithm in an HBC.

A. Tazay and Z. Miao are with the Department of Electrical Engineering, University of South Florida, Tampa, FL 33620 USA (e-mail: `zmiao@usf.edu`).

C. Organization of the Paper

The rest of the paper is organized as follows. The topology and steady-state characteristics of the three-phase HBC are described in Section II. A modified PWM using five reference signals (three-phase ac voltage signals and positive and negative dc signals) is also presented in this section. MPPT algorithm, phase-locked-loop (PLL), vector control and the battery charging scheme are presented in Section III. Section IV presents case study results to test the performance of the controller via simulation conducted in MATLAB/Simpowersystems. Section V provides the experimental results which is realized using LabView-FPGA module integrating with National Instruments Single Board RIO-9606.

II. THREE-PHASE HBC-BASED PV CHARGING STATION TOPOLOGY AND OPERATION

A three-phase HBC uses the same amount of switches as a two-level voltage source converter (VSC). However, the HBC can realize both dc/dc conversion and dc/ac conversion. As a comparison, Fig. 1 shows the conventional PV charging station where a dc/dc boost converter and a three-phase VSC are used to integrate the PV system, the PHEVs and the ac grid. A three-phase HBC replaces the two converters: the dc/dc boost converter and the dc/ac three-phase VSC to decrease the energy conversion stages and the power losses of the PV charging station. Fig. 2 shows the HBC-based PV charging station's topology. The main components of the configuration of the PV charging station consist of PV array, three-phase bidirectional HBC, ac grid, off-board dc/dc converter, and PHEV's batteries.

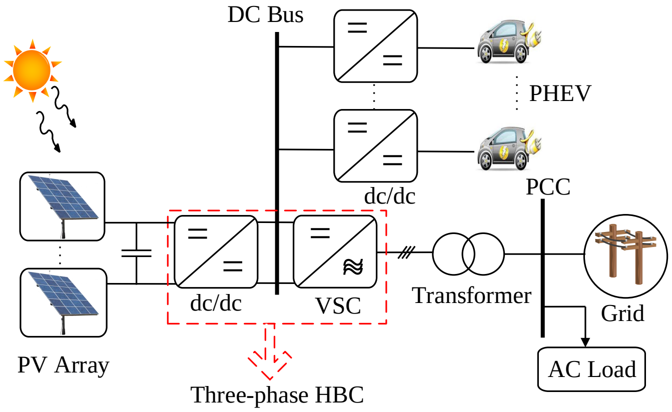

Fig. 1. Architecture configurations of a PV charging station. The conventional topology includes a dc/dc converter and a dc/ac VSC. These two converters will be replaced by a three-phase HBC.

In order to design the control of a PV charging station, it is essential to understand the operation of a three-phase HBC. Detailed operation of an HBC can be found in [10], [11], [16]. Here a brief description is given.

The system is composed of a PV array, a dc system, a three-phase ac system, and the interfacing three-phase HBC as shown in Fig. 2. The PV side includes a large inductance to achieve continuous condition and capacitance to decrease the voltage ripple. The dc side includes a diode, a dc bus for PHEV connection, a dc capacitor to eliminate the output current ripples, an off-board unidirectional isolated dc/dc converter, and PHEV batteries. The ac system includes a three-phase LC filter, a step-up transformer, and the point of common coupling (PCC) bus that connects the PV station to the main grid.

The PV array is composed of connecting series cells and parallel strings. Each PV cell has specific characteristics depending on the type and designing criteria. PV models depend mainly on Shockley diode equation [17], [18]. PV can be modeled as a photon-generated current source in parallel with a two-diode system and a shunt resistor, R_{sh}, as well as in series with a series resistor, R_s. The mathematical equations of two-diode PV cell are given in [17]. HBC-based PV charging station has the capability to operate at medium and high power ratings of such PV power plants since a single IGBT-based VSC has the capability to operate at high voltage rating (e.g., voltage limitation up to1200 V [19]).

Traditional dc/dc boost converter is operated on two modes which are "on" and "off" states. Conventional VSC is operated on "active" and "zero" modes where the output ac power can have a value or zero. The three-phase HBC integrates the operational phases of a VSC and a dc/dc converter into three main modes. The main three intervals include a shoot-through (ST) mode, an active mode (A), and a zero mode (Z).

Some assumptions are considered to better illustrate the steady-state operation of the three-phase HBC. First, the system is assumed to be lossless where the damping elements equal zero. Second, the voltage drop on the diode is very small so it can be ignored. Next, the operational mode of the three-phase HBC is operated as an inverter where the power flows from the PV into the grid. It is recognized that the three-phase HBC can be operated at converter or inverter based on the direction of power flow. Finally, the diode current is continuous during the active phase. The steady-state relations between the PV, the dc side and the ac side are given as follows.

$$V_{\rm dc} = \frac{V_{\rm pv}}{1 - D_{st}}, \quad \hat{V}_{\rm ac} = M_i \frac{V_{\rm dc}}{2} \tag{1}$$

$$V_{LL} = M_i \frac{\sqrt{3}}{\sqrt{2}} \frac{V_{\rm dc}}{2} = 0.612 \frac{M_i}{1 - D_{st}} V_{\rm pv} \tag{2}$$

where M_i and D_{st} are the ac voltage per-phase modulation index and duty cycle of the shoot-through period, $V_{\rm dc}$, $\hat{V}_{\rm ac}$, and V_{LL} are the peak dc voltage, peak per-phase ac voltage, the RMS value of the line-to-line output ac voltage, respectively. It can be concluded from (2) that the dc output depends on only D_{st} while ac output depends on both D_{st} and M_i. In order to achieve continuous control of modified PWM, the controlling signals have to achieve this condition:

$$M_i + D_{st} < 1 \tag{3}$$

A. Modified PWM

It is mentioned in Section II that the three-phase HBC is operated at three main intervals which are integrated between boost converter and VSC's phases. Conventional sinusoidal

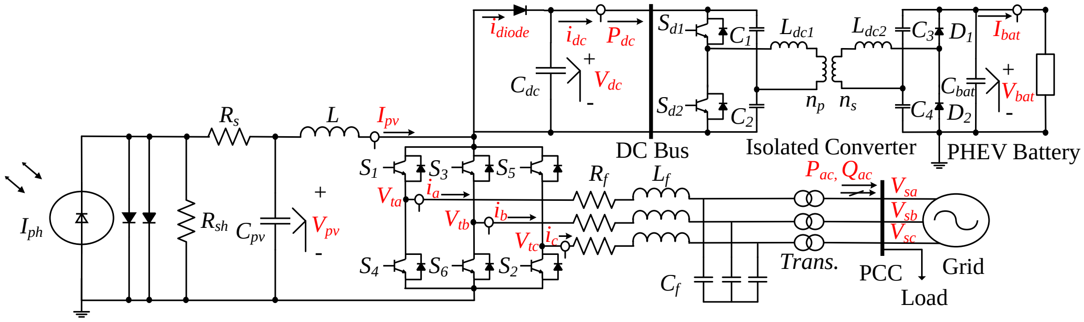

Fig. 2. Topology of the three-phase HBC-based PV charging station.

PWM and dc PWM are not appropriate to operate the switching states of three-phase HBC. Instead of separately controlling the dc and ac outputs using the switches of three-phase HBC, a modified PWM is applied to control two outputs at the same time as shown in Fig. 3. It is recommended to insert the shoot-through phase within the zero mode where the output ac power equals zero in this phase [20]. During the shoot-through period, one leg of the two switchings, e.g., S_1 and S_4 are both on. This leads to PV side current flowing into S_1, S_4 only. During the shoot-through period, the inductor L gets charged. At the zero mode, all upper-level switches S_1, S_3 and S_5 are on while the lower-level switches S_4, S_6 and S_2 are off. At this mode, the PV side current all flows to the dc side battery systems while the current to the ac system is zero. Finally, during the active mode, current will flow into the ac system.

The behavior of the open-loop control scheme for switching states of the three-phase HBC is shown in Fig. 3 when the reference for the phase voltages are related as $V_a > V_b > V_c$. The shoot-through operation occurs when the positive signal V_{st} is lower than carrier signal (phase C is shoot through with S_5 and S_2) and when the negative signal V_{st} is greater than the carrier signal (phase A is shoot-through with S_1 and S_4 on).Shoot through happens at the phases with the highest voltage or lowest voltage. In Fig. 3, phase A and Phase C are the phases with shoot-through periods. Modified PWM regulates the switching states by controlling five signals which are three-phase ac signals V_a, V_b, V_c, and dc signals V_{st} ($V_{st} = 1 - D_{st}$), and $-V_{st}$. The ac controlling signals V_a, V_b, and V_c are controlled by modulation index M_i as well as phase angles while the dc signals $+V_{st}$, and $-V_{st}$ are regulated by duty ratio D_{st}. The advantage of using modified PWM is that both dc and ac outputs can be adjusted.

III. CONTROL OF PV CHARGING STATION

This section provides a detailed explanation on the framework and controller of the HBC-based PV charging station. From the steady-state relationship in (2), three-phase HBC utilizes D_{st} to boost the PV voltage while the modulation index M_i regulates the ac voltage V_t's magnitude. In addition, the angle of the three-phase ac voltage V_t can be adjusted to achieve active power and reactive power regulation. When the ac voltage is balanced and the ac system is symmetrical, the total three-phase instantaneous power is constant at steady-state. Thus, average power of the ac side equals to the net power at the dc side ($P_{\text{ac}} = P_{\text{pv}} - P_{\text{dc}}$).

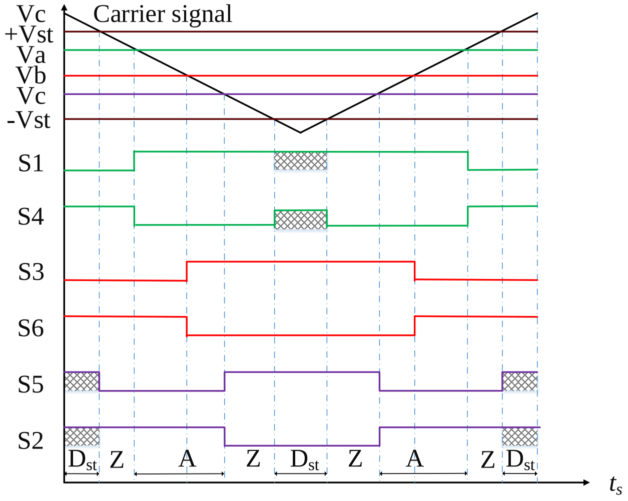

Fig. 3. A modified PWM for the three-phase-HBC. Shoot-through occurs when both switches are closed. ST, A, and Z are shoot-through, active, and zero periods, respectively.

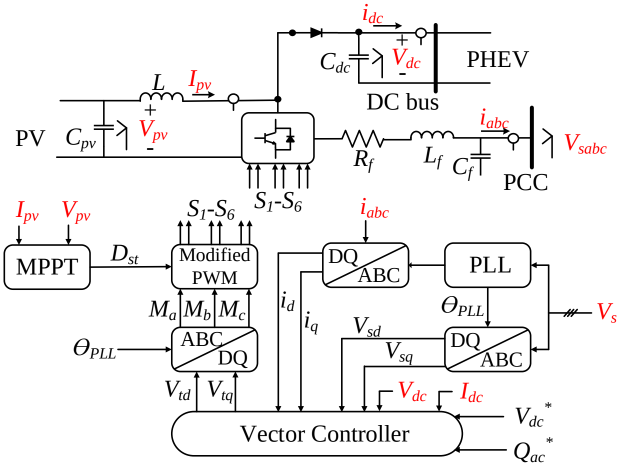

Fig. 4. Control blocks of the HBC-based PV charging station.

Three main control blocks are used to control the three-phase HBC: MPPT, phase-locked loop (PLL) and vector control as shown in Fig. 4. Each block will be described by a subsection. The charging algorithm of the off-board isolated dc/dc converter will also be addressed in this section.

A. MPPT

Maximum power point tracking (MPPT) algorithm is important to guarantee maximum power extraction from PV arrays. Various types of MPPT algorithms have been recently applied to control of MPP of PV modules. Hill climbing (HC), perturb and observe (PO), and incremental conductance (IC) are the most attractive algorithms. MPPT techniques with simple structures and fast dynamic performances are demanded. IC among other MPPT methods has the benefits of fast dynamic performance [14], [21].

IC method computes the sensitive of power variation against the PV voltage. The optimal point is achieved when $\frac{dP_{\text{pv}}}{dV_{\text{pv}}} = 0$. Fig. 5 presents current/voltage relationship and power/voltage relationship for a PV model based on Sunpower SPR-E20-327 which includes 60 parallel strings and 5 series modules in each string to generate maximum power of 100 KW. In the power/voltage plots, the maximum power points (MPPs) are located at the top of each plot when the gradient is zero. The slope is positive in the left hand side of a MPP and negative in the right hand side as shown in Fig. 5.

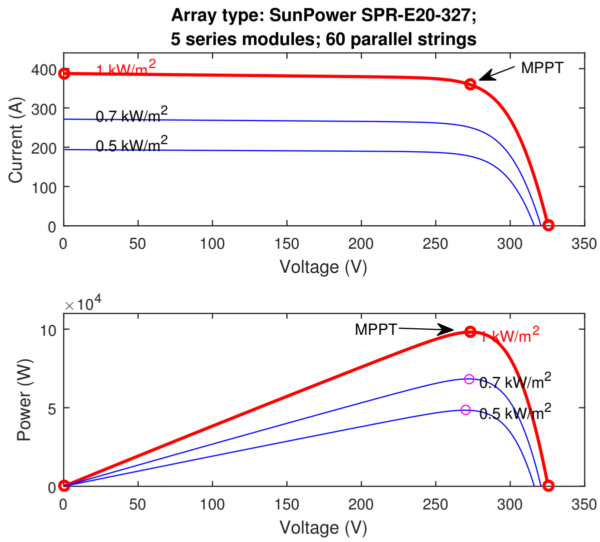

Fig. 5. IV-curve for Sunpower SPR-E20-327. (a) I-V curve. (b) P-V curve. MPP occurs at $I_{mpp} = 365$ A and $V_{\text{pv}} = 273.5$ V to generate maximum power 100 kW.

$$\frac{dP_{\text{pv}}}{dV_{\text{pv}}} = I_{\text{pv}} + V_{\text{pv}}\frac{dI_{\text{pv}}}{dV_{\text{pv}}} \begin{cases} = 0, \text{MPP} \\ > 0, \text{left slope} \\ < 0, \text{right slope} \end{cases} \tag{4}$$

Instead of using $\frac{dP_{\text{pv}}}{dV_{\text{pv}}}$ as an indicator, the incremental conductance (IC) method relies on $\frac{dI_{\text{pv}}}{dV_{\text{pv}}}$. Based on the above relationship, we can also find that the following relationship:

$$\begin{cases} \frac{\Delta I_{\text{pv}}}{\Delta V_{\text{pv}}} + \frac{I_{\text{pv}}}{V_{\text{pv}}} = 0, \text{optimal point} & (a) \\ \frac{\Delta I_{\text{pv}}}{\Delta V_{\text{pv}}} + \frac{I_{\text{pv}}}{V_{\text{pv}}} > 0, \text{left slope} & (b) \\ \frac{\Delta I_{\text{pv}}}{\Delta V_{\text{pv}}} + \frac{I_{\text{pv}}}{V_{\text{pv}}} < 0, \text{right slope} & (c) \end{cases} \tag{5}$$

The IC method requires to have the voltage deviation. When voltage deviation is very small, the computed incremental conductance may not be accurate. It is observed that the error of comparing the instantaneous conductance ($\frac{I_{\text{pv}}}{V_{\text{pv}}}$) to the incremental conductance ($\frac{\Delta I_{\text{pv}}}{\Delta V_{\text{pv}}}$) does not achieve zero at low irradiation [22].

To avoid using ΔV_{pv} in the denominator, [14] proposed a modified IC method. The modified IC method is derived based on (4):

$$\text{sign}(dV_{\text{pv}})dP_{\text{pv}} = \text{sign}(dV_{\text{pv}})(I_{\text{pv}}dV_{\text{pv}} + V_{\text{pv}}dI_{\text{pv}}) \begin{cases} = 0, \text{MPP} \\ > 0, \text{left slope} \\ < 0, \text{right slope} \end{cases} \tag{6}$$

The control block of the modified IC based MPPT is shown in Fig. 6. The instantaneous conductance will be added to the incremental conductance to generate an error signal. A proportional-integral (PI) controller forces the error signal to approach zero. The output of the MPPT block is subtracted from the reference duty cycle D^* to generate D_{st}, which further regulates the output dc voltage.

The substraction is based on the relationship between V_{pv} and V_{dc} in (1a): $V_{\text{pv}} = V_{\text{dc}}(1 - D_{st})$. When the PV operation point is located as the left slope of the power/voltage curve, we would like to have V_{pv} be increased, or D_{st} be reduced if the input signal is greater than zero. Therefore, the substraction is employed in the control block.

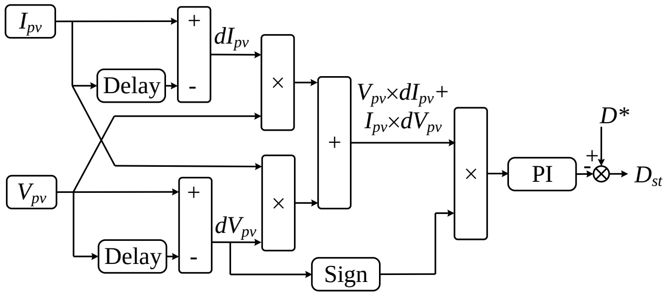

Fig. 6. MPPT technique for PV using modified incremental conductance (IC)-PI algorithm.

B. Synchronous rotating reference frame-based phase-locked-loop (SRF-PLL)

The three-phase HBC is operated at grid-tied mode since the PV charging station needs ac grid as a backup supply. Integration of the three-phase HBC has to satisfy IEEE-1547 standard which requires synchrony of the phase and angular frequency of the three-phase HBC with the main grid [23], [24]. Synchronous rotating frame-based phase-locked-loop (SRF-PLL) aligns the space vector of the point of common coupling (PCC) voltage to the d-axis and forces the q-axis PCC voltage V_{sq} to zero using a PI compensator as shown in Fig. 7.

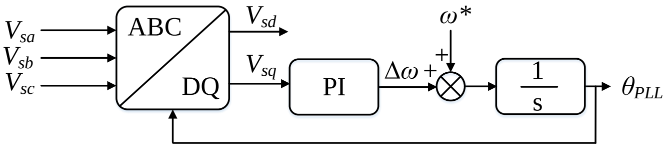

Fig. 7. Basic schematic diagram of a SRF-PLL.

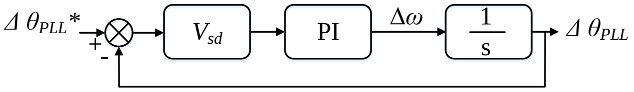

Fig. 8. Linearized model of SRF-PLL.

The open-loop transfer function is given from the linearized model of the SRF-PLL shown in Fig. 8.

$$G_{\mathrm{PLL}} = \frac{K_{p,\mathrm{PLL}} + K_{i,\mathrm{PLL}} s}{s} \frac{V_{sd}}{s} \tag{7}$$

where $K_{p,\mathrm{PLL}}$, $K_{i,\mathrm{PLL}}$, and V_s are compensator parameters and the grid's voltage amplitude, respectively. The closed-loop transfer function of SRF-PLL is a second-order system with an oscillation mode with a damping factor ζ and a natural frequency ω_n. The parameters of the compensator are selected based on selecting ζ to be $\frac{1}{\sqrt{2}}$ while ω_n to be the reference frequency of the grid ω. The resulting parameters are:

$$K_{i,\mathrm{PLL}} = \frac{\omega^2}{V_s}, \quad K_{p,\mathrm{PLL}} = \frac{2\zeta\sqrt{K_{i,\mathrm{PLL}}}}{V_s}. \tag{8}$$

C. Vector Control

Vector control technique is used for VSCs. The inner loop controls the ac current while the outer loop controls the dc voltage and reactive power. The dynamic equations of the three-phase HBC are similar to those of the conventional VSC examined in [25], [26]. The main difference of HBC is the consideration of D_{st}.

The inner current control loop is designed to respond much faster than the outer voltage controller for fast response and disturbance rejection. It is suggested to achieve fast transient response that the response of the inner loop to be in milliseconds, while the outer loop is 10 times slower than the inner loop.

The open-loop of the inner current loop includes the transfer function of the plant and the delay of the modified PWM as well as the PI compensator.

$$G_{i,ol}(s) = \left(K_{pi} + \frac{K_{ii}}{s}\right) \frac{1}{L_f s + R_f} \frac{1}{T_{\mathrm{PWM}} s + 1} \tag{9}$$

where T_{PWM} is time delay of switching frequency of the modified PWM; K_{pi} and K_{pi} are the PI compensator's parameters for the inner current loop; L_f and R_f are the inductance and resistance filter components of the converter, respectively.

Tuning current compensator is achieved by using modulus optimum technique [26]. The concept of modulus optimum is defined as shifting the dominated poles that cause slow dynamic response and achieving unity gain for the closed-loop system. The PI controller's zero will cancel the pole dominated by the RL circuit dynamics. The open-loop transfer function becomes

$$G_{iol}(s) = \frac{1}{s T_{\mathrm{PWM}} (T_{\mathrm{PWM}} s + 1)} \tag{10}$$

by choosing the following parameters: $K_{pi} = \frac{L_f}{T_{\mathrm{PWM}}}$, $K_{ii} = \frac{R_f}{T_{\mathrm{PWM}}}$.

One of the advantage of the proposed HBC-based PV station is to generate a supported reactive power to the main grid. The controlling design of the reactive power loop is explained in details. The delivered reactive power of the HBC at PCC is calculated as:

$$Q_{pcc} = -\frac{3}{2} V_{sd} i_q \tag{11}$$

where V_{sd} is the projection of the ac voltage component on d axis of the stationary reference frame; i_q is the projection of the output current of HBC on q reference frame. The open-loop transfer function of the reactive power controller is given as follow:

$$\begin{aligned} G_{ol}(s) &= G_Q(s) G_{pi}(s) G_{sw}(s) G_i(s) \\ &= \left(\frac{3}{2} V_{sd}\right) \left(\frac{k_{pQ} s + k_{iQ}}{s}\right) \left(\frac{1}{T_{\mathrm{PWM}} s + 1}\right) \left(\frac{1}{L_f s + R_f}\right) \end{aligned} \tag{12}$$

where k_{pQ} and k_{iQ} are the PI compensator's parameters. Using modulus optimum technique on Equ. (12), the open-loop and closed loop transfer functions of the reactive power equation are driven as:

$$G_{ol}(s) = \frac{1}{\tau_Q s (T_{\mathrm{PWM}} s + 1)} \tag{13}$$

$$G_{cl}(s) = \frac{1}{T_{\mathrm{PWM}} \tau_Q s^2 + \tau_Q s + 1} \tag{14}$$

$$k_p = \frac{3}{2} \frac{V_{sd} L_f}{\tau_Q}; k_i = \frac{3}{2} \frac{V_{sd} R_f}{\tau_Q} \tag{15}$$

where τ_Q is the time constant of the resultant closed-loop system. Equation (14) represents a general form of the second order system. The frequency of natural oscillation is obtained from (14) to be equal $\omega_n = \sqrt{\frac{1}{T_{\mathrm{PWM}} \tau_Q}}$ while the damping factor equals $\zeta = \sqrt{\frac{\tau_Q}{4 T_{\mathrm{PWM}}}}$.

Assuming there is no switching power loss, the steady-state operation of power balance relationship of the three-phase HBC is given as:

$$P_{\mathrm{pv}} = P_{\mathrm{cap}} + P_{\mathrm{dc}} + P_{\mathrm{ac}} \tag{16}$$

$$P_{\mathrm{ac}} = \frac{3}{2} V_{sd} i_d \tag{17}$$

where i_d and V_{sd} are the projections of the ac current and grid voltage space vectors on the d-axis.

The power relationship is further expressed as follows.

$$\begin{aligned} P_{\mathrm{cap}} = C V_{\mathrm{dc}} \frac{d V_{\mathrm{dc}}}{dt} &= P_{\mathrm{pv}} - P_{\mathrm{ac}} - P_{\mathrm{dc}} \\ &= V_{\mathrm{dc}} I_{\mathrm{pv}} - \frac{3}{2} V_{sd} i_d - V_{\mathrm{dc}} I_{\mathrm{dc}} \end{aligned}$$

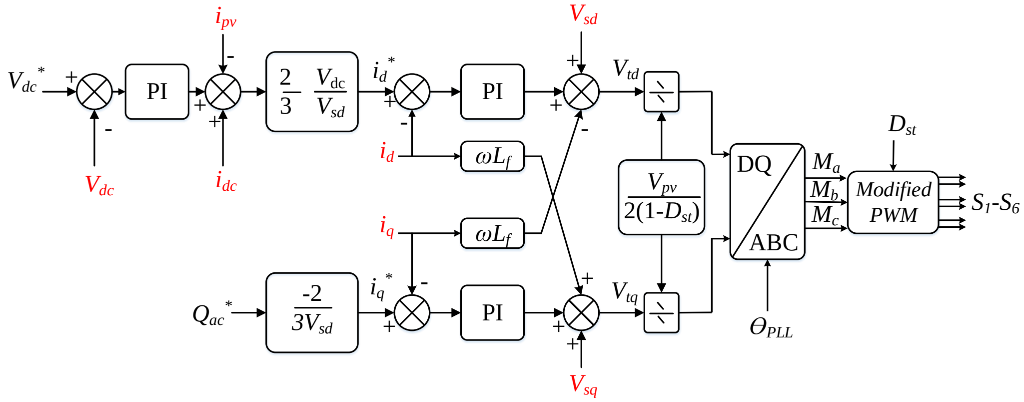

Fig. 9. Vector control scheme of the three-phase HBC.

Therefore, the dynamics of the capacitor voltage can be expressed as follows.

$$C\frac{dV_{\rm dc}}{dt} = \underbrace{I_{\rm pv} - \frac{3}{2}\frac{V_{sd}}{V_{\rm dc}}i_d - I_{\rm dc}}_{u_d} \tag{18}$$

A negative feedback controller will be designed to take in the dc voltage error $V_{\rm dc}^* - V_{\rm dc}$ and amplified by a PI controller. The output of the PI controller is u_d. From this signal, the reference signal i_d^* will be generated as:

$$i_d^* = \frac{2}{3}\frac{V_{\rm dc}}{V_{sd}}(u_d - I_{\rm pv} + I_{\rm dc}).$$

The open-loop transfer function of outer voltage is given as:

$$G_{v,ol}(s) = \left(K_{pv} + \frac{K_{iv}}{s}\right)\frac{1}{\tau_i s + 1}\frac{1}{Cs} \tag{19}$$

where τ_i is the time constant for the inner current closed loop. The open-loop transfer function for voltage controller includes two poles at origin.

Symmetrical optimum is a technique to deal with an open-loop system with double integrators [26]. The concept of symmetrical optimum is to operate the system at a low frequency to slow down the dynamic response which leads to an increased phase margin. The compensator parameters are given based on the symmetrical optimum method as follows.

$$T_{iv} = a^2\tau_i, \quad K_{\rm pv} = \frac{C}{K\sqrt{T_{iv}\tau_i}}, \quad K_{iv} = \frac{K_{\rm pv}}{T_{iv}} \tag{20}$$

where K equals $\frac{3V_{sd}}{2V_{\rm dc}}$ and a is the symmetrical frequency range between peak phase margin and low frequency operation area. It is important to select a high value of the symmetrical gain a to achieve high phase margin. The value of a falls between 2 and 4 [27].

D. Off-board Battery Charger Control

Most of the PHEV manufactures use lithium-ion batteries to operate their vehicles (e.g., Chevy Volt and Nissan Leaf). An equivalent electrical battery cell model is shown in Fig. 11. The battery model is composed of capacitor $C_{Capacity}$ and a current-controlled current source that represent the battery's life. It also includes the Thevenin-based model of the transient and steady state elements as well as an voltage-controlled open circuit voltage source. The controllable voltage source is dependent on the amount of available energy or state of charge (SOC) in battery cells.

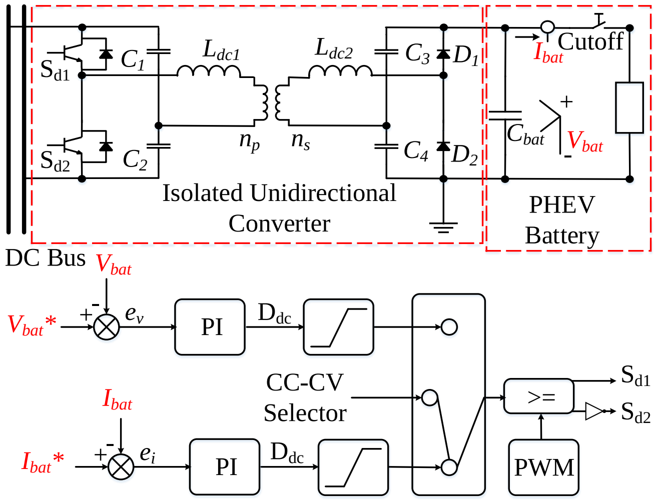

Fig. 10. A single battery cell circuit model with off-board charging structure using CC-CV algorithm .

An aggregated model of PHEV battery is used in the paper. Fig. 11 demonstrates the equivalent circuit of connecting PHEV batteries to the PV charging station. The battery's cells are connected in series to increase the voltage of the battery while the parallel connection of the battery cells increases the total energy. Each PHEV's battery consists of M branches and each branch consists of N cells. The aggregated model is shown in Fig. 11. The detailed parameters of the commercial PHEV can be found in [28].

There are several types of PHEV charging schemes: constant voltage (CV), constant current (CC), and taper-current (TC). Constant voltage (CV) method does not require an off-board dc/dc converter. CV can be realized through the HBC's vector control, which regulates the dc-link voltage.

Off-board unidirectional isolated dc/dc converter is adopted

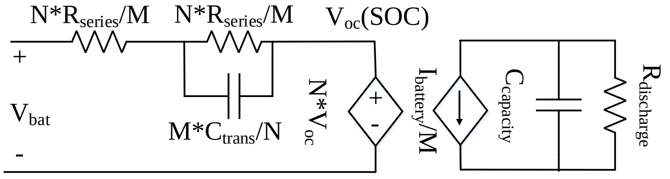

Fig. 11. Equivalent circuit of a PHEV Li-ion battery module.

to realize optimal charging scheme using both CV and CC [29], [30]. In this paper, we adopted the off-board dc/dc converter with optimal charging to increase the performance and life cycle of the battery as well as to minimize the damage of the PHEV's batteries caused by fast charging.

For safety consideration, isolation of the PHEV's battery with respect to the grid terminal and the PV power source is important for battery protection. Several safety codes and standards such as SAE J-2344, SAE J-2464, UL 2202, and IEC TCs-64 recommend an isolation function for charging the PHEV's battery. The charging station should provide a fully galvanic isolation of the PHEV's battery towards the main distribution network and the dc bus at the PV station. Since the isolated on-board chargers are usually avoided due to the weight and cost, isolated off-board is required for safety considerations. A high-frequency transformer is implemented on the off-board converter to isolate the PHEV's battery from the rest of the system during charing period. The advantages of this topology include better voltage adjustment control and more safety for the PHEV's battery. The configuration of off-board charging converter includes an isolated unidirectional half-bridge converter is shown in Fig. 10.

Since a battery storage system is one of the most critical and expensive elements of PHEV, charging control needs to be carefully designed especially for fast charging process of PV stations. Fast charging technique may cause an excessive damage to the battery at the beginning of the charging process or an increase in the cell temperature if the battery reaches full charge and high current charging is continued [31]. Hence we need to consider these aforementioned consequences in controlling and designing PV charging stations.

In terms of charging schemes of an PHEV's battery, constant-current (CC) charging, constant-voltage (CV) charging, and taper-current (TC) charging are the three basic types for charging the batteries [32]–[34].

The CC charging method performs a relatively uniform current charging without considering the battery state of charging (SOC) or temperature. The CC method mainly depends on low or high constant charging current which helps to eliminate imbalance among cells and enhances life cycle of the battery. However, low charging current may not be suitable for fast charing while high charging current could easily catalyzes excessive damage.

The CV procedure generally limits the voltage input to a specific level regardless of the SOC of the battery. Implementing CV method requires the knowledge of initial battery's voltage to avoid the high initial current due to high potential difference between the battery and the charger. This requirement is difficult to comply in real applications of PV stations since PHEVs have different battery characteristics.

The TC charging method depends on decreasing the charging current proportionally to the voltage rising in the battery. The advantage of this method is that it prevents the gasification and overheating issues. However, this method is difficult to implement in the real applications due to the different characteristics of PHEV's batteries.

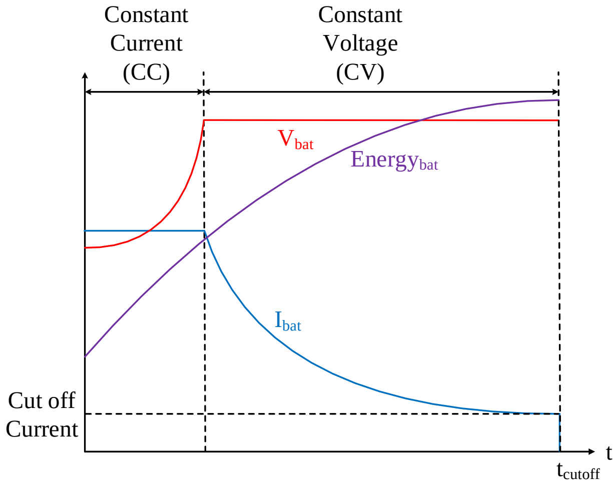

Fig. 12. A simple illustration of CC-CV technique for PHEV's battery charging.

Considering the features of the aforementioned methods, this paper introduces the integration of CC and CV methods to enhance the efficiency and reliability of the PV charging station. The procedure of implementing CC-CV in a dc/dc converter is shown in Fig. 12. The charging process first charges the battery with a constant current to avoid high initial current using the CV method. When the battery's voltage reaches the rated battery's voltage, the controller switches to the CV method to avoid overcharge. Finally, when the battery's energy reaches the full charged region and the battery's current reaches the cut-off line, the controller disconnects the PHEV for protection. Implementing CC-CV method for PV fast charging station has several advantages such as avoiding overheating and preventing overcharge.

When the charging procedure is operated at CC mode, the dc/dc converter charges the battery with a constant current until the voltage reaches its preset value. Then, the control method is changed to the CV mode to supply a constant voltage. Finally, when the battery current reaches the cut-off current, the dc/dc converter disconnects the PHEV's battery to avoid overcharge. Fig. 10 shows two control loops are used to regulate the measured components of the battery and the configuration of the detailed PHEV battery and off-board dc/dc buck converter. The goal of the selector is to choose the operational mode of the charger and to disconnect the battery when it is fully charged.

The performance of the CC-CV charging method is tested on the proposed system and shown in Fig. 13. The CC method is first selected for fast dc charging with 40 A. The battery is continuously charged until it reaches 360 V (the rated battery

This article has been accepted for publication in a future issue of this journal, but has not been fully edited. Content may change prior to final publication. Citation information: DOI 10.1109/TEC.2018.2812181, IEEE Transactions on Energy Conversion

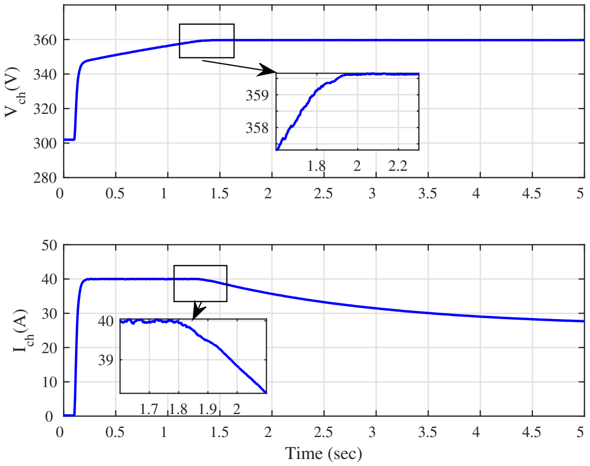

Fig. 13. Performance of CC-CV algorithm.

TABLE I
SYSTEM PARAMETERS

	Parameters		Parameters
PV	$V_{oc} = 65.1$ V $V_{mpp} = 54.7$ V $I_{sc} = 6.46$ A $I_{mpp} = 5.98$ A $R_{sh} = 298.531\ \Omega$ $R_s = 0.369\ \Omega$	AC	V_{grid}(L-L) $= 20$ kV $\omega = 377$ rad/s $S = 100$ kVA V_t(L-L) = 208 V $R_f = 2$ mΩ $L_f = 125\ \mu$H $C_f = 150\ u$F
DC	$V_{\text{dc}} = 350$ V $L = 5$ mH $C = 12000\ \mu$F $Load = 100$ kW $L_{dc} = 10$ mH $C_{dc} = 100\ \mu F$	Control	$K_{pi} = 0.625\ \Omega$ $K_{ii} = 10\ \Omega$/s $K_{\text{pv}} = 0.24\ \Omega^{-1}$ $K_{iv} = 300\ \Omega^{-1}/s$ $K_{pvdc} = 0.001$ $K_{ivdc} = 25$ $K_{iidc} = 0.001$ $K_{iidc} = 3$
Chevy	# of Cells: 200 $V_{\text{cell}} = 1.25$ V $Q_{\text{energy}} = 16$ kWh Type: Li-Ion	Nissan	# of cells: 160 $V_{\text{cell}} = 1.875$ V $Q_{\text{energy}} = 24$ kWh Type: Li-Ion

voltage of Chevy Volt vehicle). When the battery voltage reaches 360 V at 1.5 seconds, the CV control is selected while the battery's current is gradually decreasing to the cut-off region. This method is applied for each vehicle in the PV charging station.

IV. SIMULATION RESULTS

Case studies for a PV charging station using a three-phase HBC with the proposed control are conducted in MATLAB/SimPowerSystems environment. The system's parameters and PV data are given in Table I. The data for the PV model are based on PV array type Sunpower SPR-E20-327. The V-I and P-V curves for different irradiance values are shown in Fig. 5. The battery parameters of Chevrolet Volt and Nissan Leaf are used to represent the batteries of PHEVs [6], [35], [36]. Five case studies are conducted to evaluate MPPT and vector control as well as to illustrate the operation modes of the PV charging station.

A. Case 1: Performance of the Modified Incremental Conductance-PI MPPT

The goal of this case study is to validate the performance of the modified MPPT using incremental conductance-PI algorithm. According to Fig. 5, the maximum PV power is 100 kW when the PV array generates 273.5 V at 1 kW/m^2 solar irradiance. Fig. 14 shows the performance of MPPT when the system is subject to solar irradiance variation.

The dc voltage V_{dc} and the PV voltage V_{pv} are related based on the duty cycle ratio D_{st} that is generated from MPPT. The role of vector controller is to keep the dc voltage V_{dc} at its reference value $350V$ and supply reactive power Q^*_{ac} to the ac grid. The role of MPPT algorithm is to adjust the duty cycle ratio D_{st} and in turn adjust the PV output voltage V_{pv} so that the PVs are operating at the maximum power extracting point.

Fig. 14 provides the performance of MPPT based on four different intervals. From $0 - 0.5$ seconds, the sun irradiance is 0.9 kW/m^2 and the MPPT control is not activated. The output PV power supplies approximately 70 kW. At $t = 0.5$ seconds, MPPT is activated, the duty cycle ratio is decreased and the PV voltage is improved. This in turn improves the PV power output to be 90 kW. Note that whether the MPPT is on or off, V_{dc} is kept at 350 V.

At $t = 1$ second and $t = 1.5$ seconds, the sun irradiance increases and decreases. Due to the MPPT control, the optimal PV output voltage is kept at the optimal level. Further, the PV output power tracks the maximum point at each irradiance level.

Fig. 14 validates the good tracking performance of MPPT when different solar irradiations are applied to the PV. The simulation results also show that the vector controller can regulate the dc voltage at 350 V and reject disturbances.

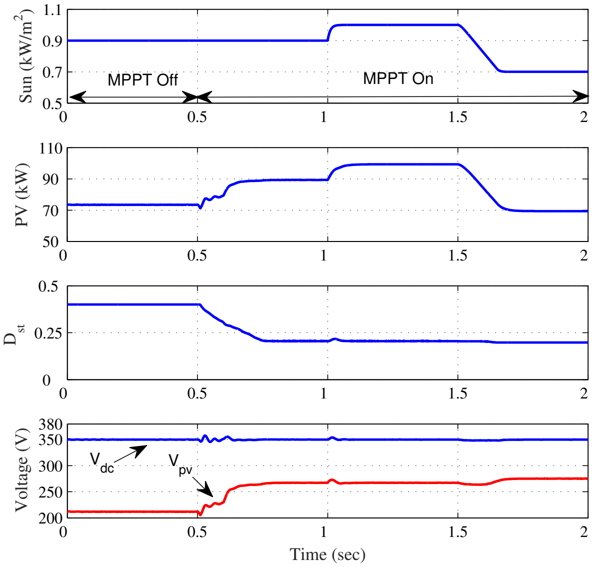

Fig. 14. Performance of a modified IC-PI MPPT algorithm when solar irradiance variation is applied.

B. Case 2: Performance of the DC voltage controller

The advantages of implementing the three-phase HBC on PV charging station is its capability to supply dc and ac power simultaneously. The main objective of a PV charging station is to supply continuous dc power to electric vehicles. Case 2 investigates the ability of the proposed controller to provide constant dc voltage with PV power variation and MPPT control status change. As a comparison, a system with dc voltage control disabled is also simulated. For this system, the reference d-axis current is kept constant.

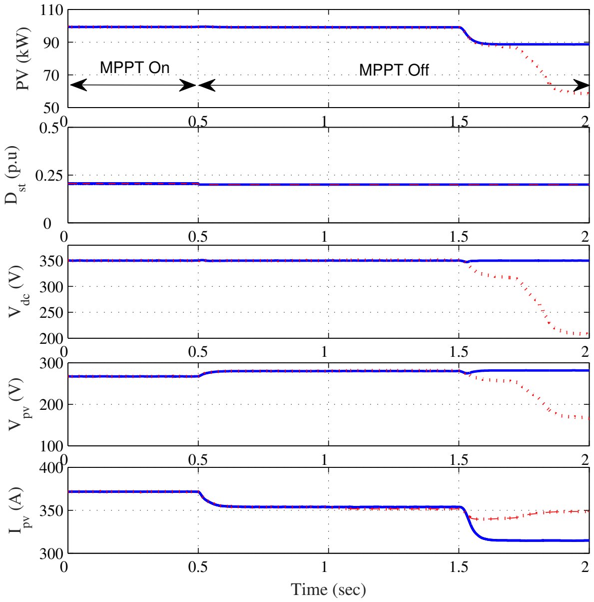

Fig. 15. Performance of the dc voltage control in the vector control. The solid lines represent the system responses when the dc voltage control is enabled. The dashed lines represent the system responses when the dc voltage control is disabled.

Fig. 15 shows that when the dc voltage control is enabled, whether the MPPT control is on or off and whether the PV power has change or not, the dc voltage V_{dc} is kept at 350 V.

As a comparison, when the dc voltage control is disabled and the MPPT control is off, when the PV power is subject to a change, the PV voltage will vary. Since the MPPT control is off, the duty cycle ratio D_{st} is kept constant and the dc voltage V_{dc} varies as well.

This case study shows that the dc voltage control in the vector control provides an additional measure to keep the dc voltage constant.

C. Case 3: Performance of reactive power control

Another advantage of the three-phase HBC control is that it can support the ac grid by supplying or absorbing reactive power. The vector controller of PV charging station using three-phase HBC is well designed in previous sections to achieve decouple controlling for real and reactive power. This feature is applied in this case study to investigate the ability of the vector controller to quickly track the reactive power reference as well as maintain a constant dc voltage.

The system is first in steady-state and the vector controller regulates the dc voltage and supply ac power at unity power factor as shown in Fig. 16. At $t = 0.5$ seconds the reference reactive power absorbs 10 kVAr while at $t = 1$ seconds it is changed to supply 20 kVAr to the main ac grid. The controller shows a good performance to track the reactive power reference as well as regulate the dc voltage at 350 V. Fig. 16 illustrates that the vector controller's M_d and M_q respond to the reactive power variation as well as main a constant dc voltage. It also shows that the dc voltage and reactive power can be controlled independently.

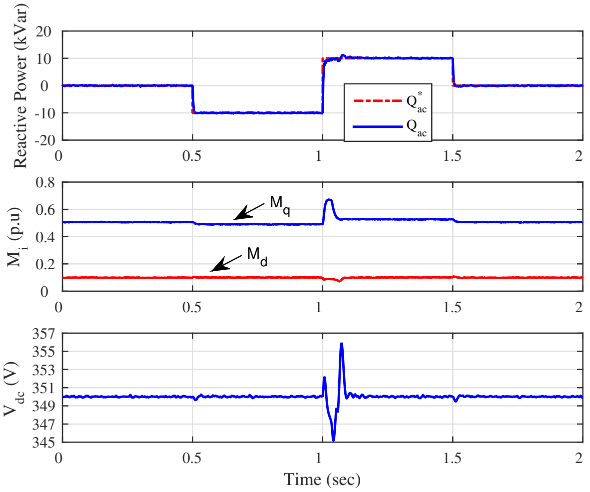

Fig. 16. Performance of a proposed vector control to supply or absorb reactive power independently.

D. Case 4: Power management of the PV charging station

An objective of the three-phase HBC is to charge PHEVs even when there is not enough PV power. The performance of the PV charging station is evaluated when different values of solar irradiation are applied. The main goal of this case study is to show continuous charging PHEVs even when the PV power is low. At day time the solar irradiance is assumed to be 1 kW/m^2 while at sun set the irradiance decreases to 0.7 kW/m^2.

The dc load first consumes 50 kWh which represents charging of two Nissan Leaf vehicles. The two Nissan Leafs are charged before the PV power decreases as shown in Fig. 17. The remaining of PV power transfers to the main grid. At $t = 0.5$ seconds, the PV power reduces due to irradiance change. Two more vehicles are connected to the system consequently at $t = 1$ seconds and $t = 1.5$ seconds. Fig. 17 shows that the PV array can provide power to the third car at $t = 1.5$ seconds. The PV power is used to charge the batteries of PHEV with no dependency on the main grid.

At $t = 1.5$ seconds, the fourth electric car (Chevy Volt 2) is connected to the system. The bidirectional feature of the three-phase HBC and the regulated dc voltage controller allow the dc load to absorb power from the main grid to charge the fourth vehicle as shown in Fig. 16. It is also noticed that the three-phase HBC can achieve power balance as well as maintain constant dc voltage at 350 V.

Fig. 17 also shows that the reactive power Q_{ac} is kept at 0. This shows that the three-phase HBC can achieve decoupled control of real and reactive power. Fig. 18 presents the duty cycle ratio and the modulation index in dq-axes. Fig. 19 presents the detailed control signals for modified PWM and the resulting switching sequences.

This case study demonstrates that the proposed control can provide smooth transition when HPEVs are connected into the PV charging station.

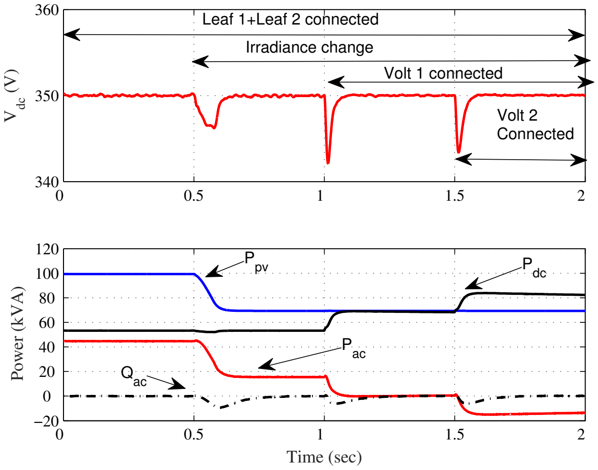

Fig. 17. Power management of PV charging station.

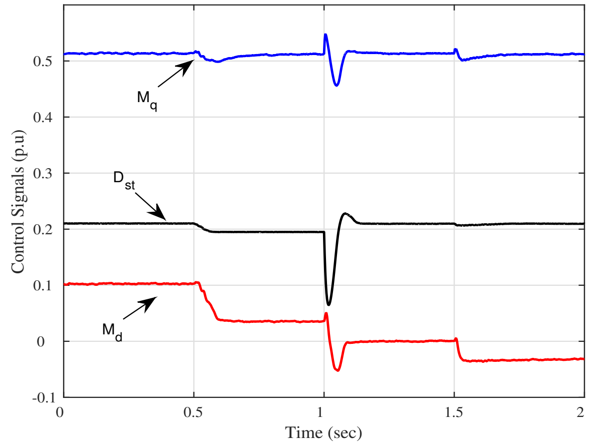

Fig. 18. D_{st}, M_d and M_q for case 4.

E. Case 5: Partial grid failure

The controller design of the three-phase HBC based PV charging station can take care of the partial grid failure. The controller is designed to provide a stable dc voltage even when grid fault is occurred. Generally, when the main grid voltage sages below 80% of the nominal voltage, the power quality standards recommend to disconnect the charged PHEV to protect the battery's life cycle [37]. The goal of designing the PV charging station's controller is to achieve constant charging procedure when a fault is occurring at the main grid. The method of is to provide sufficient power to charge the PHEV's batteries as well as to maintain a constant dc-link voltage. As a result, it is unnecessary to disconnect the PHEVs during grid fault. The capability of partial grid failure tolerance is demonstrated in the following case study.

The PV charging station is first connected to the main grid where the PHEV's batteries are charged during the steady-state period. MPPT is enabled at $t = 0.5$ seconds. A symmetrical 70% voltage sag is occurred at $t = 1.0$ seconds. Normally, it is recommended to disconnect the ac load as well as the PHEV's batteries for protection and safety. However, the proposed controller can mitigate this issue by stabilizing the dc-link voltage at its rated value as well as generating the required power to the local ac load. As can be seen in Fig. 20, the controller of the PV charging station can stabilize the dc bus voltage at its rated value. As shown in Fig. 20, the generated real power from the PV station (P_{pv}) is kept the same (100 kW) due to MPPT control. The PHEV load (60 kW) is kept the same since the dc-bus voltage is kept the same. In turn, the power right after the HBC P_{HBC} to the ac side is kept the same (40 kW). The 70% reduction in the ac voltage reduces the load power consumption from 20 kW to decreased to 10 kW. In turn, the power to the grid P_{ac} is increased to 30 kW.

At $t = 1.5$ seconds, the voltage recovers to 1 pu and the powers return to the values before 1 seconds.

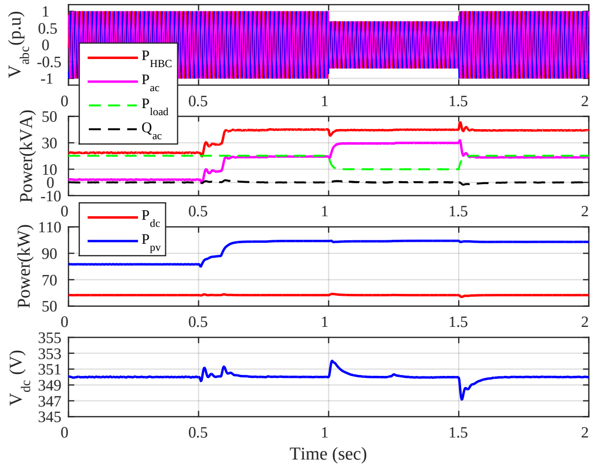

Fig. 20. System performance under 70% grid's voltage drop.

V. EXPERIMENTAL RESULTS

The behavior of the proposed PHEV charging station has been validated using a laboratory prototype. National Instruments (NI) Single-Board RIO-9606 and a NI General Purpose Inverter Controller (GPIC) are used to validate the topology of the HBC-based PV charging station. The LabView field-programmable gate array (FPGA) performs signal processing, data analysis, and system controlling using a host computer. The system's controller is implemented using LabView-FPGA to drive the switches of the HBC as well as monitor the charging procedure of the battery. It also provides a system's protection by monitoring the thermal behavior of the HBC as well as disconnecting the battery when a fault occurs. NI-GPIC board measures the real-time data of the power inverter and executes the controlling signals. The exchanged information

This article has been accepted for publication in a future issue of this journal, but has not been fully edited. Content may change prior to final publication. Citation information: DOI 10.1109/TEC.2018.2812181, IEEE Transactions on Energy Conversion

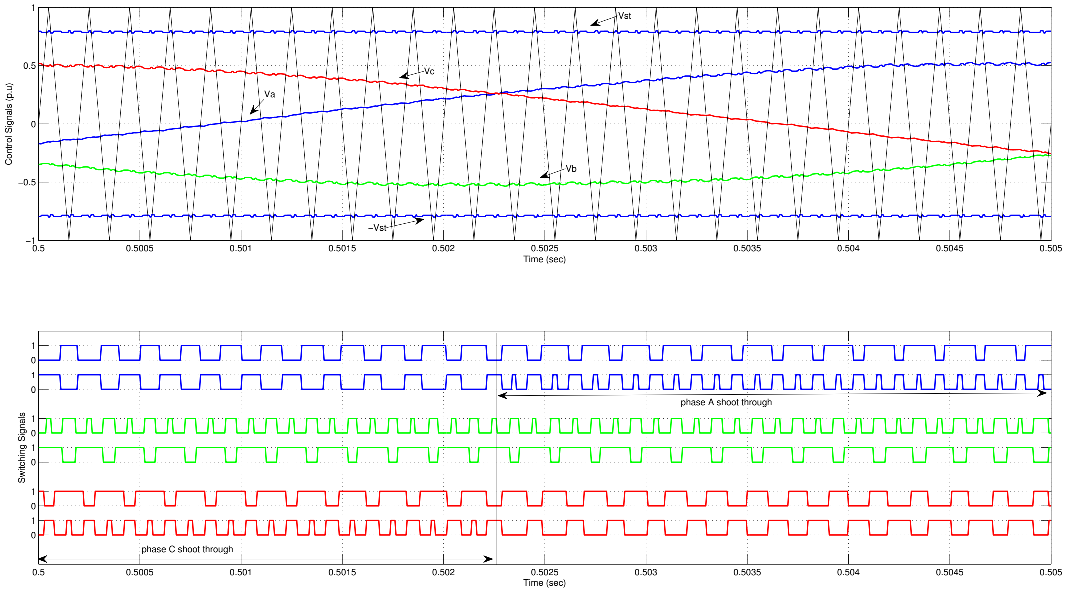

Fig. 19. The modified PWM signals and the switching sequences.

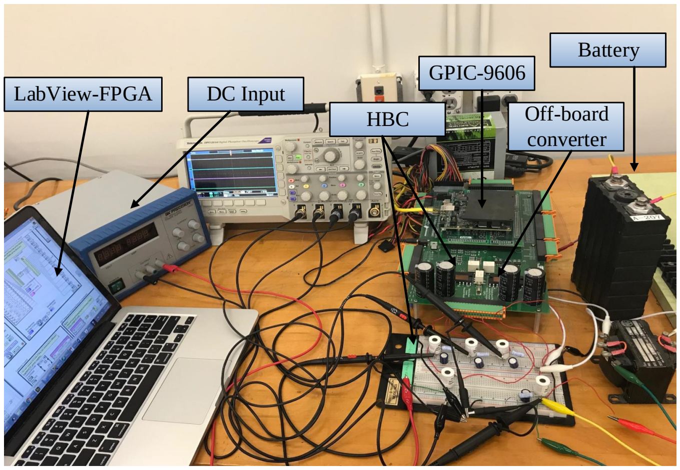

Fig. 21. Experimental setup for laboratory prototype of the charging station.

between the host application on LabView-FPGA and the NI-GPIC is realized by Ethernet network.

A laboratory PHEV charger is constructed to validate the topology and operation of the system in this paper. For safety reasons, the power rating is downscaled due to the limitation of the actual battery and the NI-GPIC. Fig. 21 shows the laboratory setup of the PHEV charging station. The layout of the experimental testing is categorized into five main parts, including NI Single-Board GPIC RIO-9606, NI-GPIC back-back inverters, a host LabView-FPGA computer, dc power supply, and dc and ac loads. The NI-GPIC back-back inverters contain two inverters which are used for the HBC topology and off-board dc/dc converter. The configuration of the HBC requires adjusting the topology of the NI-GPIC back-back inverters since the research board contains only three-phase IGBT-based inverters. The detailed configurations of the HBC and off-board converters are given in Fig. 22. The dc load contains Lithium-ion battery which mimics the PHEV's battery. Sinopoly SP-LFP40AHA Lithium-ion battery is used for the experimental testing which is connected to the off-board dc/dc converter for performing a charging procedure. The programmable dc source is used for replacing the PV power source. The ac output filter contains LC components to

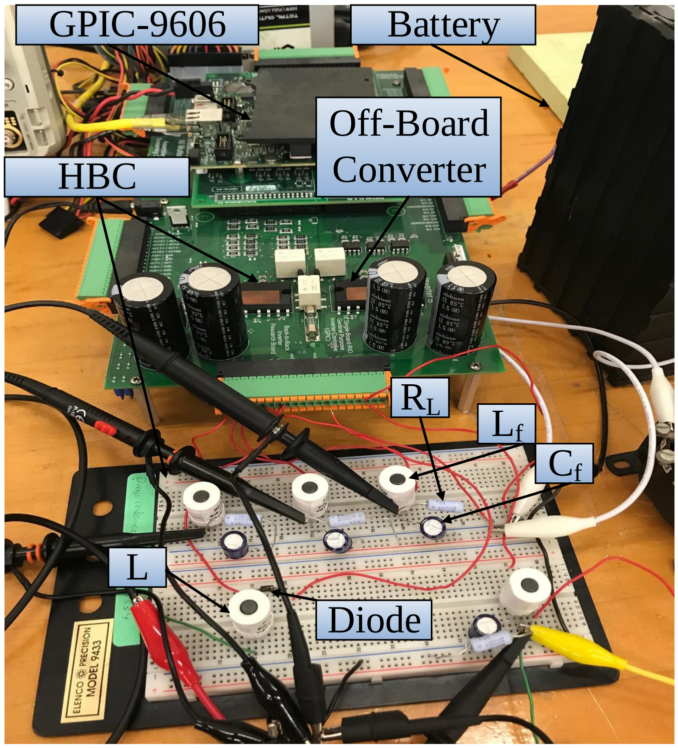

Fig. 22. Detailed laboratory configuration of the HBC and off/board converter.

TABLE II
PARAMETERS OF THE LABORATORY PHEV CHARGER.

System Parameters AC side	Value	System Parameters DC side	Value
AC frequency	377 rad/second	V_{pv}	10 V
HBC F_{sw}	5 kHz	DC/DC F_{sw}	10 kHz
L_f	5.6 mH	DC-link voltage	20 V
C_f	47 μF	C_{pv}	47 μF
$\hat{V}_{\text{ac}}$	$5V_{\text{peak}}$	L	5.6 mH
R_L	30 Ω	Li-ion Voltage	3.2 V
K_{pdc}	0.5	K_{idc}	0.001

filter out the high-frequency components of the output signals. The ac side is connected to a resistive load R_L. The list of parameters and downscaled values of the laboratory PHEV charger are given in Table. II.

The control scheme of the HBC-based PV charging station has been applied in LabView-FPGA to drive the switches of the HBC. A closed-loop control for V_{dc} is used to control the dc bus voltage by regulating the D_{st} as given in Fig. 23.

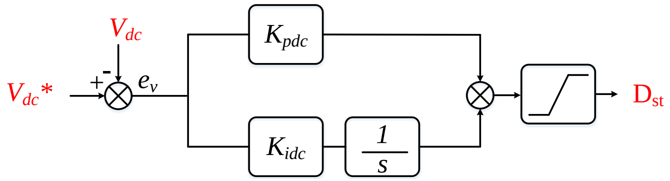

Fig. 23. Closed-loop control for dc bus voltage. $K_{pdc} = 0.5$, $K_{idc} = 0.001$.

The controlled signal D_{st} is then applied to the modified PWM to define the shoot-through period. The dc input source can generate both dc and ac power outputs. Fig. 24 shows the steady-state output waveforms from a single input dc source. The three-phase ac outputs are fed to a three-phase balanced load while the dc power is used to charge the battery at the dc bus. Fig. 24 shows that the input 10 V dc can generate 20 V dc and 5 V peak per-phase voltage $\hat{V}_{\text{abc}}$ when D_{st} and M_i are 0.5 and 0.25, respectively. It can be seen that the summation of D_{st} and M_i is less than 1, which satisfies the operation of the modified PWM.

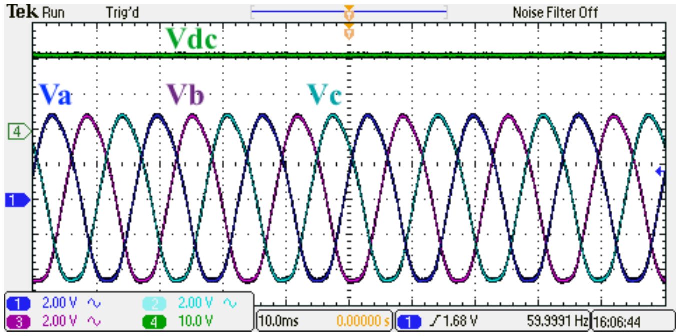

Fig. 24. Steady state output waveforms for HBC. The V_{dc} equals 20 V at while the value of D_{st} equals 0.5. The peak phase $\hat{V}_{abc}$ equals 5 V at 0.25 of M_i.

According to (2), the peak per-phase ac voltage depends on both D_{st} and M_i. Figs. 25 and 26 show a step change in the output dc voltage from 1 V to 20 V leading to an increase in the D_{st} as well as an increase in the output ac voltage. The output signal D_{st} from the V_{dc} closed-loop controller changes from 0.33 to 0.5 (shown in Fig. 25) while the value of M_i keeps constant.

Fig. 27 shows the behavior of phase a when a step change in the M_i is applied from 0.2 to 0.25 which leads to change the $\hat{V}_{\text{ac}}$ from 4 to 5 V while the dc-link voltage remains constant as 20 V. As indicted by (1), regulating M_i leads to change in the ac output voltage but not in dc output voltage. Figs. 26 and 27 verify (1) and (2).

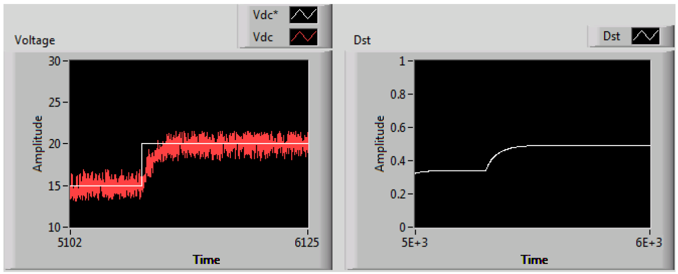

Fig. 25. Performance of closed-loop voltage using LabView-FPGA when the reference V_{dc} is changed from 15 V to 20 V.

VI. CONCLUSION

Control of three-phase HBC in a PV charging station is proposed in this paper. The three-phase HBC can save switching loss by integration a dc/dc booster and a dc/ac converter converter into a single converter structure.

A new control for the three-phase HBC is designed to achieve MPPT, dc voltage regulation and reactive power tracking. The MPPT control utilizes modified incremental conductance-PI based MPPT method. The dc voltage regulation and reactive power tracking are realized using vector control.

Five case studies are conducted in computer simulation to demonstrate the performance of MPPT, dc voltage regulator, reactive power tracking and overall power management of the PV charging station. Experimental results verify the operation of the PHEV charging station using HBC topology. The simulation and experimental results demonstrate the effectiveness and robustness of the proposed control for PV charging station to maintain continuous dc power supply using both PV power and ac grid power.

ACKNOWLEDGEMENT

The authors wish to express their gratitude towards Prof. Lingling Fan for her suggestions and comments.

REFERENCES

[1] M. Ehsani, Y. Gao, and A. Emadi, *Modern electric, hybrid electric, and fuel cell vehicles: fundamentals, theory, and design*. CRC press, 2009.
[2] K. Sikes, T. Gross, Z. Lin, J. Sullivan, T. Cleary, and J. Ward, "Plug-in hybrid electric vehicle market introduction study: final report," Oak Ridge National Laboratory (ORNL), Tech. Rep., 2010.

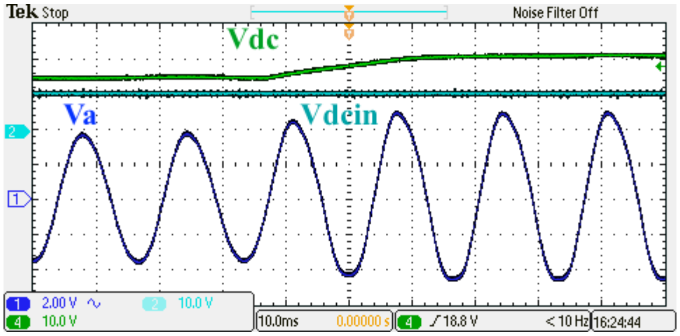

Fig. 26. A step change on the dc voltage. V_{dc} is changed from 15 V to 20 V which leads to modify the D_{st} from 0.33 to 0.5. The peak $\hat{V}a$ is also increased from 4 V to 5 V because of V_{dc} variation. The value of the M_i remains constant at 0.25 during the V_{dc} step change.

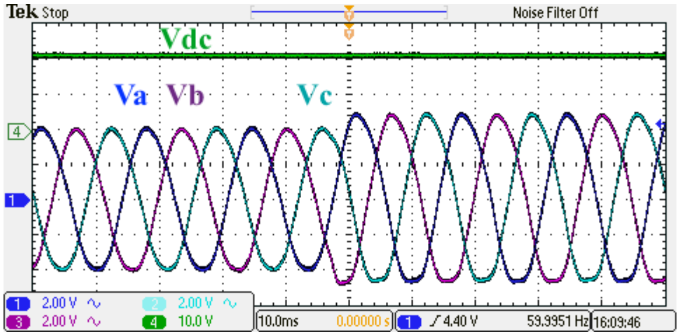

Fig. 27. A step change on the M_i. The output peak $\hat{V}_{abc}$ is changed from 4 V to 5 V by varying the M_i from 0.2 to 0.25. The V_{dc} remains constant before and after a step change at 20 V. The value of the D_{st} keeps fixed at 0.5 during the variation of M_i.

[3] A. Khaligh and S. Dusmez, "Comprehensive topological analysis of conductive and inductive charging solutions for plug-in electric vehicles," *IEEE Transactions on Vehicular Technology*, vol. 61, no. 8, pp. 3475–3489, 2012.

[4] T. Anegawa, "Development of quick charging system for electric vehicle," *Tokyo Electric Power Company*, 2010.

[5] F. Musavi, M. Edington, W. Eberle, and W. G. Dunford, "Evaluation and efficiency comparison of front end ac-dc plug-in hybrid charger topologies," *IEEE Transactions on Smart grid*, vol. 3, no. 1, pp. 413–421, 2012.

[6] M. Yilmaz and P. T. Krein, "Review of battery charger topologies, charging power levels, and infrastructure for plug-in electric and hybrid vehicles," *IEEE Transactions on Power Electronics*, vol. 28, no. 5, pp. 2151–2169, May 2013.

[7] G. Gamboa, C. Hamilton, R. Kerley, S. Elmes, A. Arias, J. Shen, and I. Batarseh, "Control strategy of a multi-port, grid connected, direct-dc pv charging station for plug-in electric vehicles," in *Energy Conversion Congress and Exposition (ECCE), 2010 IEEE*. IEEE, 2010, pp. 1173–1177.

[8] P. Goli and W. Shireen, "Pv integrated smart charging of phevs based on dc link voltage sensing," *IEEE Transactions on Smart Grid*, vol. 5, no. 3, pp. 1421–1428, 2014.

[9] S. Mishra, R. Adda, and A. Joshi, "Inverse watkins–johnson topology-based inverter," *IEEE Transactions on Power Electronics*, vol. 27, no. 3, pp. 1066–1070, 2012.

[10] O. Ray and S. Mishra, "Boost-derived hybrid converter with simultaneous dc and ac outputs," *IEEE Transactions on Industry Applications*, vol. 50, no. 2, pp. 1082–1093, March 2014.

[11] O. Ray, V. Dharmarajan, S. Mishra, R. Adda, and P. Enjeti, "Analysis and pwm control of three-phase boost-derived hybrid converter," in *2014 IEEE Energy Conversion Congress and Exposition (ECCE)*, Sept 2014, pp. 402–408.

[12] O. Ray and S. Mishra, "Integrated hybrid output converter as power router for renewable-based nanogrids," in *Industrial Electronics Society, IECON 2015 - 41st Annual Conference of the IEEE*, Nov 2015, pp. 001 645–001 650.

[13] M. A. Elgendy, B. Zahawi, and D. J. Atkinson, "Assessment of perturb and observe mppt algorithm implementation techniques for pv pumping applications," *IEEE transactions on sustainable energy*, vol. 3, no. 1, pp. 21–33, 2012.

[14] J. Khazaei, Z. Miao, L. Piyasinghe, and L. Fan, "Real-time digital simulation-based modeling of a single-phase single-stage pv system," *Electric Power Systems Research*, vol. 123, pp. 85–91, 2015.

[15] M. Tabari and A. Yazdani, "Stability of a dc distribution system for power system integration of plug-in hybrid electric vehicles," *IEEE Transactions on Smart Grid*, vol. 5, no. 5, pp. 2564–2573, 2014.

[16] O. Ray and S. Mishra, "Integrated hybrid output converter as power router for renewable-based nanogrids," in *Industrial Electronics Society, IECON 2015-41st Annual Conference of the IEEE*. IEEE, 2015, pp. 001 645–001 650.

[17] U. Eicker, *Solar technologies for buildings*. John Wiley & Sons, 2006.

[18] N. Femia, G. Petrone, G. Spagnuolo, and M. Vitelli, *Power electronics and control techniques for maximum energy harvesting in photovoltaic systems*. CRC press, 2012.

[19] M. R. Patel, *Wind and solar power systems: design, analysis, and operation*. CRC press, 2005.

[20] O. Ellabban, J. V. Mierlo, and P. Lataire, "Comparison between different pwm control methods for different z-source inverter topologies," in *Power Electronics and Applications, 2009. EPE '09. 13th European Conference on*, Sept 2009, pp. 1–11.

[21] T. Esram, P. L. Chapman *et al.*, "Comparison of photovoltaic array maximum power point tracking techniques," *IEEE Transactions on Energy Conversion EC*, vol. 22, no. 2, p. 439, 2007.

[22] C. Dorofte, U. Borup, and F. Blaabjerg, "A combined two-method mppt control scheme for grid-connected photovoltaic systems," in *Power electronics and applications, 2005 European conference on*. IEEE, 2005, pp. 10–pp.

[23] "Ieee standard for interconnecting distributed resources with electric power systems," *IEEE Std 1547-2003*, pp. 1–28, July 2003.

[24] D. Dong, B. Wen, D. Boroyevich, P. Mattavelli, and Y. Xue, "Analysis of phase-locked loop low-frequency stability in three-phase grid-connected power converters considering impedance interactions," *IEEE Transactions on Industrial Electronics*, vol. 62, no. 1, pp. 310–321, Jan 2015.

[25] A. Yazdani and R. Iravani, *Voltage-sourced converters in power systems: modeling, control, and applications*. John Wiley & Sons, 2010.

[26] A. Tazay, Z. Miao, and L. Fan, "Blackstart of an induction motor in an autonomous microgrid," in *2015 IEEE Power Energy Society General Meeting*, July 2015, pp. 1–5.

[27] F. Fröhr and F. Orttenburger, *Introduction to electronic control engineering*. Heyden, 1982.

[28] Y. Hu, S. Yurkovich, Y. Guezennec, and B. Yurkovich, "A technique for dynamic battery model identification in automotive applications using linear parameter varying structures," *Control Engineering Practice*, vol. 17, no. 10, pp. 1190–1201, 2009.

[29] C. C. Grant, *US National Electric Vehicle Safety Standards Summit: Summary Report*. Fire Protection Research Foundation, 2010.

[30] "Electric vehicle and plug-in hybrid electric vehicle conductive charge coupler," *SAE J1772*, Jan 2010.

[31] P. Fan, B. Sainbayar, and S. Ren, "Operation analysis of fast charging stations with energy demand control of electric vehicles," *IEEE Transactions on Smart Grid*, vol. 6, no. 4, pp. 1819–1826, July 2015.

[32] D. Linden, "Handbook of batteries and fuel cells," *New York, McGraw-Hill Book Co., 1984, 1075 p. No individual items are abstracted in this volume.*, vol. 1, 1984.

[33] M. S. Rahman, M. Hossain, and J. Lu, "Coordinated control of three-phase ac and dc type ev–esss for efficient hybrid microgrid operations," *Energy Conversion and Management*, vol. 122, pp. 488–503, 2016.

[34] J. Y. Yong, V. K. Ramachandaramurthy, K. M. Tan, and J. Selvaraj, "Experimental validation of a three-phase off-board electric vehicle charger with new power grid voltage control," *IEEE Transactions on Smart Grid*, 2016.

[35] N. Leaf, "2011 leaf owner's manual revised," 2011. [Online]. Available: http://www.nissan-techinfo.com/refgh0v/og/leaf/2011-nissan-leaf.pdf

[36] G. Motors, "2016 chevrolet volt battery system," 2016. [Online]. Available: https://media.gm.com/content/dam/Media/microsites/product/Volt_2016/doc/VOLT_BATTERY.pdf

[37] "Ieee standard for performance criteria and test methods for plug-in (portable) multiservice (multiport) surge-protective devices for equipment connected to a 120 v/240 v single phase power service and metallic

This article has been accepted for publication in a future issue of this journal, but has not been fully edited. Content may change prior to final publication. Citation information: DOI 10.1109/TEC.2018.2812181, IEEE Transactions on Energy Conversion

conductive communication line(s)," *IEEE Std C62.50-2012*, pp. 1–63, Sept 2012.

Ahmad Tazay received the master degree from University of South Florida (USF) in May 2014 and joined the USF Smart Grid Power Systems Lab in Aug. 2014 for Ph.D. study. He obtained his Ph.D. candidacy in Fall 2016 and his research interests include modeling and control of distributed energy resources and microgrids.

Zhixin Miao is with the University of South Florida (USF), Tampa. Prior to joining USF in 2009, he was with the Transmission Asset Management Department with Midwest ISO, St. Paul, MN, from 2002 to 2009. His research interests include power system stability, microgrid, and renewable energy.